Computers and Electronics in Agriculture 215 (2023) 108444

Contents lists available at ScienceDirect

Computers and Electronics in Agriculture

journal homepage: www.elsevier.com/locate/compag

Palmer amaranth identification using hyperspectral imaging and machine learning technologies in soybean field

Billy Graham Ram [a], Yu Zhang [a], Cristiano Costa [a], Mohammed Raju Ahmed [a], Thomas Peters [b], Amit Jhala [c], Kirk Howatt [b], Xin Sun [a,*]

[a] Department of Agricultural and Biosystems Engineering, North Dakota State University, Fargo, ND 58108, USA
[b] Department of Plant Sciences, North Dakota State University, PO Box 6050, Fargo, ND 58108-6050, USA
[c] Department of Agronomy and Horticulture, University of Nebraska-Lincoln, NE 68583-0915 USA

ARTICLE INFO

Keywords:
Palmer amaranth
Hyperspectral imaging
Machine learning
Multivariate data analysis

ABSTRACT

Weed infestation and their management are a critical production challenge in agricultural fields. Palmer amaranth has created management challenges because it has multiple emergence pattern and has evolved resistant to nine unique herbicide sites of action. Effective Palmer amaranth detection and positive identification in field conditions will help to improve Palmer amaranth control. A field-based hyperspectral imaging system was developed to record Palmer amaranth in soybean fields. The data were pre-processed applying Savitzky-Golay 2nd derivative, Multiplicative Scatter Correction, and Standard Normal Variate in a forward feed manner. Recursive feature elimination, SelectFromModel, sequential forward selection, and backward elimination were used to select significant wavebands from the available 224 bands. Later, supervised machine-learning models were generated to classify soybean and Palmer amaranth using the selected wavebands. Matthew's correlation coefficient (MCC), F1 score, precision, and recall were considered as the most significant parameters to evaluate the models' performance. The highest result was obtained by quadratic discriminant analysis with a prediction accuracy of 93.95%, a precision of 90.30%, a recall of 90.29%, an F1 score of 0.95, and an MCC score of 0.85. The findings of this study showed that the combination of hyperspectral imaging and machine-learning is a potential technique for real-time weed detection in the open field condition.

1. Introduction

Palmer amaranth poses a serious threat to soybean production due to its extended germination and emergence, rapid growth and competitiveness with cultivated crops, and water use efficiency that increases farmers' expenses and workload (Klingaman and Oliver, 2017). Its invasiveness has been confirmed to reduce soybean crop yields up to 78 % compared to soybean grown in a weed-free environment (Bensch et al., 2003). In a study on competition between soybean and Palmer amaranth conducted by Monks and Oliver (1988), it was found that Palmer amaranth at a 50-cm distance from the soybean crop can reduce its yield. Furthermore, Palmer amaranth's ability to produce male and female flowers on separate plants (dioecious) combined with its tremendous seed-producing capability have resulted in seeds with mutations that are resistant to many common herbicides used by soybean growers. Palmer amaranth has evolved resistance to acetolactate synthase (ALS)-inhibitors, microtubule assembly inhibitors, EPSP synthase inhibitors, hydroxyphenylpyruvate dioxygenase (HPPD)-inhibitors, and photosystem II inhibitor herbicides in some parts of the United States, along with multiple herbicide-resistant biotypes (Chahal et al., 2015). Competition between weeds and plants is predicated on their germination time (i.e., how fast crops and weeds germinate and emerge) to gain an initial advantage in competing for water and nutrients (Zhang et al., 2012a). Horak and Loughin (2000) also reported that Palmer amaranth growth parameters were greater than those of other Amaranthaceae species, including waterhemp, redroot pigweed, and tumble pigweed. Effective and early detection of Palmer amaranth is therefore crucial for its control in the soybean field.

Different species of pigweed in the Amaranthaceae family look very similar, especially when they are small and subsequently easiest to control. Making proper identification at this stage crucial. Hyperspectral imagery (HSI) is one technique that can allow differentiation between similar plants based on their light reflective properties (Thomas et al., 2018). Spectroscopy enables hyperspectral imagery to detect small variations in the absorption and reflectance of certain wavelengths of

* Corresponding author.
E-mail address: xin.sun@ndsu.edu (X. Sun).

https://doi.org/10.1016/j.compag.2023.108444
Received 20 March 2023; Received in revised form 30 October 2023; Accepted 15 November 2023
Available online 26 November 2023

Nomenclature

ALS	Acetolactate synthase
CH	Carbon Hydrogen Bond
EPSP	5-Enolpyruvylshikimate-3-phosphate
FN	False Negative
FP	False Positive
HPPD	4-Hydroxyphenylpyruvate dioxygenase
HSI	Hyperspectral Imaging
KNN	K-Nearest Neighbor
MCC	Matthew's Correlation Coefficient
ML	Machine Learning
MSC	Multiplicative Scatter Correction
NIR	Near Infrared
NNC	Neural Network Classifiers
PA	Precision Agriculture
PTFE	Polytetrafluoroethylene
RFE	Recursive Feature Elimination
RGB	Red Green Blue
ROI	Region of Interest
SBE	Sequential Backward Elimination
SFM	SelectFromModel
SFS	Sequential Forward Selection
SG	Savitzky Golay
SNV	Standard Normal Variate
SVM	Support Vector Machine
SWIR	Shortwave Infrared
TN	True Negative
TP	True Positive
VNIR	Visible Near Infrared

the electromagnetic spectrum (Fernández Pierna et al., 2012). Hyperspectral sensors capture wavelengths that are mostly, but not limited to, visible near infrared (VNIR) and short-wave infrared (SWIR). HSI is a powerful technique that can provide chemical information based on the unique spectral signature of the sample, hence this technique has been used to detect diseases in plants, soil mineralogy, crop monitoring, nutrient application and product sorting (Mishra et al., 2017).

Hyperspectral images have high spectral resolution that reflects the chemical composition of the subject due to the inherent properties of how different wavelengths interact with different chemical compounds in comparison with digital (RGB) images (Pavia et al., 2014). Machine learning (ML) models trained on RGB images rely more on the spatial difference (texture) among objects for training. These ML models can differentiate between objects of different colors and texture, however they fail to differentiate objects with the same color and similar spatial features due to their low spectral resolution (Farooq et al., 2019). As mentioned earlier, it is crucial to identify weeds at an early growing stage for timely and accurate weed management, during the early growth stage, plants look very similar in terms of their spatial characteristics but differ in spectral characteristics (Zhang et al., 2012b). Hyperspectral sensors overcome this limitation of RGB images by recording high spectral resolution. This facilitates hyperspectral sensors to record small variations in the absorption and reflection of chemical compounds (Atsmon et al., 2022). The use of such high-end sensors for agricultural purposes has greatly increased with the dawn of precision agriculture (PA) (Lu et al., 2020), a specialized field in agricultural engineering that leverages the use of computers and sensors to solve agricultural problems. ML, a subset of artificial intelligence, is one such innovative and effective tool in PA. ML requires a large amount of data for the algorithm to learn, and this requirement is easily fulfilled by hyperspectral images due to its high-dimensional data. Studies of weed segmentation, identification, and classification based on hyperspectral imaging methods are a target for exploration in the research community (Li et al., 2021). Classification of Palmer amaranth and other pigweed species using multispectral sensors in the greenhouse environment may enable Palmer amaranth detection under field conditions (Basinger et al., 2022). Initial research based on the theory of hyperspectral imaging technology and ML mechanism for Palmer amaranth detection and classification was first conducted in the greenhouse environment in 2019 (Costa et al., 2022).

Despite the recent advancements in weed detection using hyperspectral and RGB images, there remains a significant gap in the literature. Existing studies have primarily focused on highly curated datasets, where weed images are captured with sparse distribution and minimal overlap (Matzrafi et al., 2017). As a result, current RGB models are limited in their ability to differentiate between classes based on spatial differences alone, and struggle when faced with spatially similar weeds such as wheat and grass (Xu et al., 2021). Furthermore, there is a notable lack of research exploring the use of HSI for differentiating between Palmer amaranth and soybean in natural, highly occluded populations. This represents a critical area for future investigation. In-field hyperspectral data collection depicts practical applications for generating ML classification models and is therefore more desirable, since early weed management is the best practice for weed relief. The use of hyperspectral imaging sensors in field conditions is challenging due to sensor sensitivity and the time needed for hyperspectral data collection. The objectives of our study were to (1) develop an efficient hyperspectral data collection platform focusing to use in the open field condition; (2) hyperspectral image acquisition using the developed platform for naturally growing Palmer amaranth weeds in commercial soybean fields; (3) Machine-learning based model development to classify soybean and Palmer amaranth.

2. Materials and method

2.1. Semi-automated hyperspectral imaging system development

Hyperspectral data collection was carried out using an in-house fabricated platform. To curb the challenges of field data collection, a semi-automatic platform was constructed. It was used to record hyperspectral data using a push-broom scanner. The platform had a translation stage that could be moved in both horizontal and vertical directions, which helped in setting up the swath width of the sensor. The platform was manually pushed in the field for data collection, this platform ensured the repeatability of the procedure and made the data collection process easier. The sensor was mounted on the linear stage, which had a horizontal coverage distance of 1.5 m. The linear stage was powered by a single precision stepper motor (MDI1FRD17A4-EQ, Schneider Electric Intelligent Motions Systems, USA). The sensor frame was mounted with two halogen bulbs of 50 Watts each from opposite sides of the sensor frame that moved along with the sensor for uniform lighting of the subject. The platform, along with the data recording computer (CPU: Intel i7, RAM: 16 GB, HDD: 1 TB), was powered by 120 Volts of power generated by a 1200-Watt generator. A tarp was used to block the sunlight while data scanning was in process to reduce the adverse effects of external sunlight on the hyperspectral data. Fig. 1 shows the platform without the tarp and Fig. 2 shows a simplified illustration of the platform.

A pushbroom Hyperspectral imaging (HSI) sensor (Spectral Imaging Ltd. Oulu, Finland) was used for image acquisition. This sensor has a wavelength range of 400 –1000 nm in the VNIR regions, a mean spectral resolution of 5.5 nm and a spatial resolution of 1024 pixels, which allows it to capture spectral information in 224 bands at a 30-fps frame rate with a 38-degree field of view. This sensor operates in a line

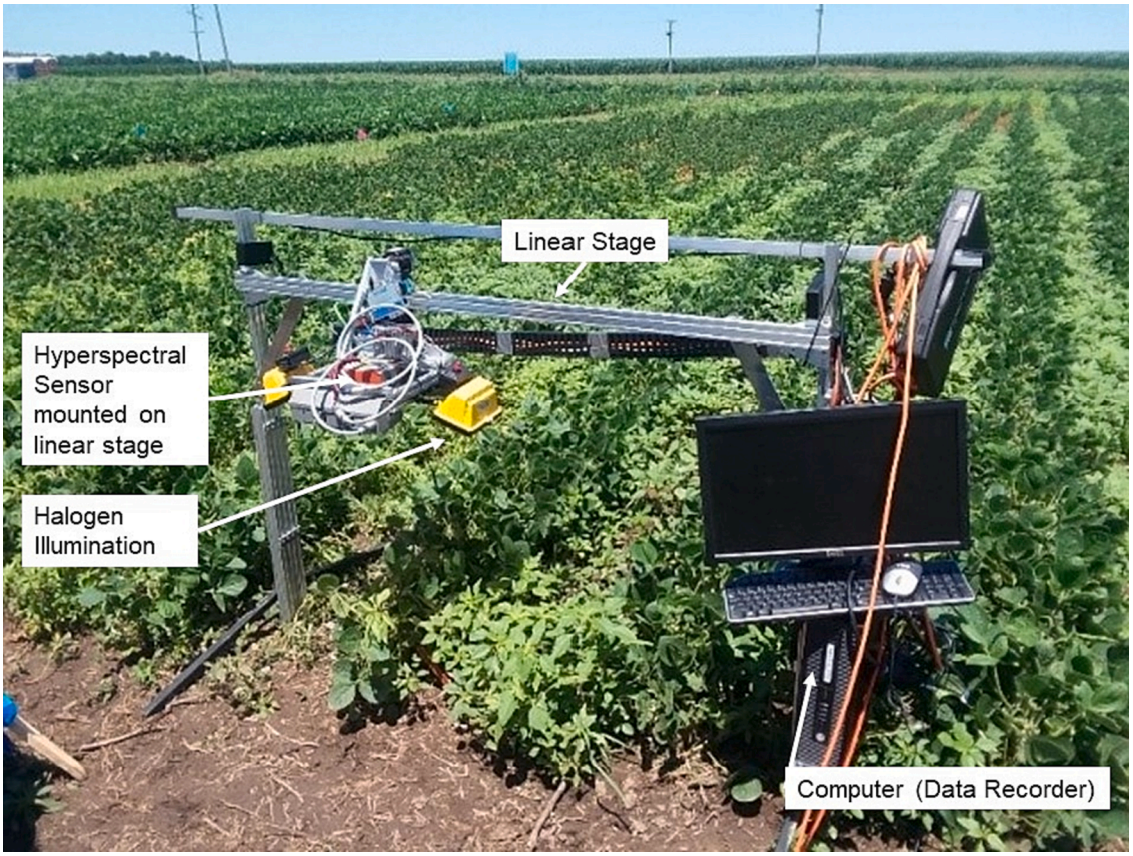

Fig. 1. Hyperspectral imaging platform used for data collection shown without tarp.

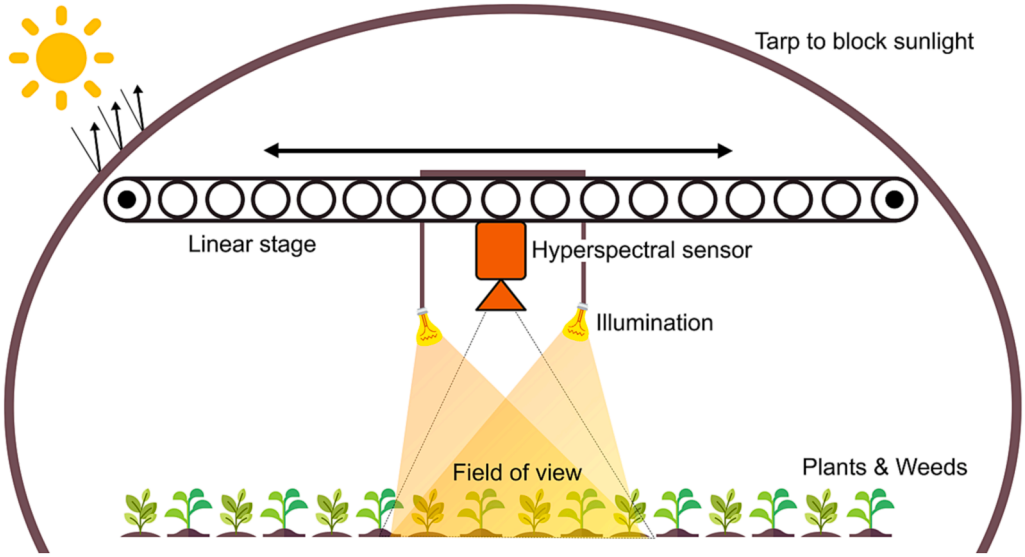

Fig. 2. Illustration of the Hyperspectral Data collection platform used in the field.

scanning method and moves during the translation stage to capture the entire image. Lumo Scanner software (Spectral Imaging Ltd. Oulu, Finland) was used to control the sensor and the translation stage. The software also collects white and dark reference images with each data image that is used for image calibration.

2.2. Data collection

Hyperspectral field data were collected on July 10–12, 2019, in a commercial soybean field near Carleton, Nebraska [40.2992° N, 97.6787° W] with a field size of 400 x 900 ft^2, as well as at the U.S. Meat Animal Research Center near Clay Center [40.5217° N, 98.0553° W] with a field size of 400 x 250 ft^2 in Nebraska, USA (Fig. 3). Both fields had indigenous populations of Palmer amaranth with a plant density of 8 plants/m^2. Data was collected when the Palmer amaranth plants reached a height of 4 in. and the soybean plants were three weeks post-sowing. In total, 61 hyperspectral images were captured, with each image taking an average of one minute to record.

Fig. 3. The study area for this research. (a) Commercial soybean field in Carleton, Nebraska. (b) U.S. Meat Animal research center, Clay Center, Nebraska.

2.3. Image calibration

The instrument was calibrated with a maximum reflectance image (also called the white reference image) along with the instrument background signal (also called the dark reference image), since the raw uncalibrated image obtained from the sensor is affected by non-uniform sensor noise and background illumination (Piqueras et al., 2012). The sensor captured the white and dark reference images during each data scanning. To capture the dark reference image, the sensor captured a closed shutter image and then captured the white reference image by scanning a calibration board (SphereOptics GmbH, Gewerbestraße, Germany), which is made up of polytetrafluoroethylene (PTFE) and reflects 95 % of incident light, making it a suitable choice for the white reference image (Noviyanto and Abdulla, 2019). The calibrated image was obtained by Eq. (1).

$$I = \frac{I_0 - I_d}{I_w - I_d} \quad (1)$$

Here$I$ is the calibrated spectral reflectance image, I_o is the raw spectral image, I_d is the dark reference image, and I_w is the white reference image. A row-wise average of dark reference image and white reference image was calculated, and these row-wise averages are used with the above-mentioned calibration formula in a row-wise pattern on the raw image to calculate the calibrated image. This is because the detectors on the HSI sensor used in this study are placed in a line, and because using a row-wise calibration pattern helps to individually correct each detector responses.

2.4. Hyperspectral image data preparation

Since Palmer amaranth was native to both fields, the areas with soybean and Palmer amaranth in proximity were scanned. A total of 61 HSI images were captured, 28 of which were collected in Clay Center and 33 of which were collected in Carleton. Image processing was done with the help of an open source MATLAB toolbox HYPER-Tools (Mobaraki and Amigo, 2018). Images had a large scan area and captured multiple soybean and Palmer amaranth plants in a single image, which ensured an image of large size. Prior to cropping, each hyperspectral cube measured 512 pixels by 685 pixels in the spatial domain and encompassed 224 distinct wavelengths. A smaller region of interest (ROI) was selected to reduce computational load and increase the amount of the dataset to aid ML training. The 61 calibrated HSI images were spatially cropped, and ROI were selected, resulting in 211 soybean images and 371 Palmer amaranth images. These ROIs had a spatial dimension in the range of 50 pixels to 100 pixels and 224 wavelengths. Segmentation was a challenging task since the field images included numerous foreign objects in addition to soybean and Palmer amaranth. K-means clustering was used to mask the image and remove the ground and other unnecessary objects from the background. Clusters values in the range of 3–5 were tested and used to effectively separate classes based on a false color image of the hyperspectral cube generated by the toolbox. Once K-means clustering had grouped most of the clusters, small areas in the image that remained as blobs were removed using morphological operations such as erosion and dilation. Fig. 4 shows an illustration of this process. This final, spatially cropped, segmented image was used to extract spectral values through the process of image unfolding (i.e., converting a multidimensional array to a table format) (Fig. 5) and the data was saved in a standard text document (.txt) as a delimited table format. During the unfolding process, the spatial resolution was removed while the full spectral resolution of 224 bands was retained. To facilitate future reference, spatial resolution information was preserved in the form of logical masks, enabling the refolding of the images. These files were saved in folders created separately for each class (soybean and Palmer amaranth). These text files were used to create data stores that were used for preprocessing, feature selection, and ML training and testing.

2.5. Data preprocessing

Preprocessing can be divided into two categories: (1) reference dependent, and (2) reference independent (Rinnan et al., 2009). The data preprocessing applied to this work used reference independent operations. The raw spectral data is often affected by light scattering due to the object's physical and the sensor's internal properties. This scattering introduces non-linearities in the data, also known as multiplicative scale effects and popularly known as scatter effects. To correct these effects, normalization was applied to the data. Two kinds of normalization methods were used in this work: multiplicative scatter correction (MSC) and standard normal variate (SNV) (Martens et al., 1983). MSC was used to remove scaling effect and baseline shift effects (Yoon and Park, 2015). MSC was applied in two steps because it requires a reference spectrum, which in this case is the spectral mean. In the first step, a correction coefficient was calculated using a linear regression equation:

$$x_i = a\bar{x} + b \quad (2)$$

where x_i is the spectrum of the sample, $\bar{x}$ is the reference spectrum (mean), and a and b are the correction coefficients. The second step was to calculate the corrected spectra (i.e., x_{corr}) using the following equation:

$$x_{corr} = \frac{x_i - b}{a} \quad (3)$$

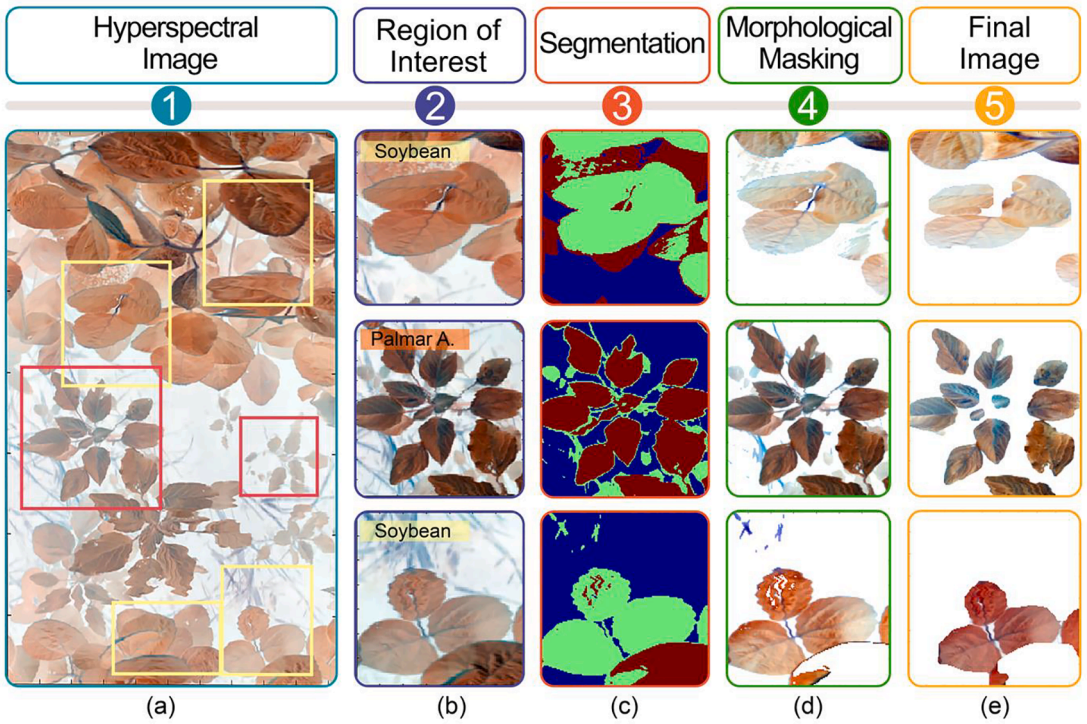

Fig. 4. Illustration of Hyperspectral image data preparation.

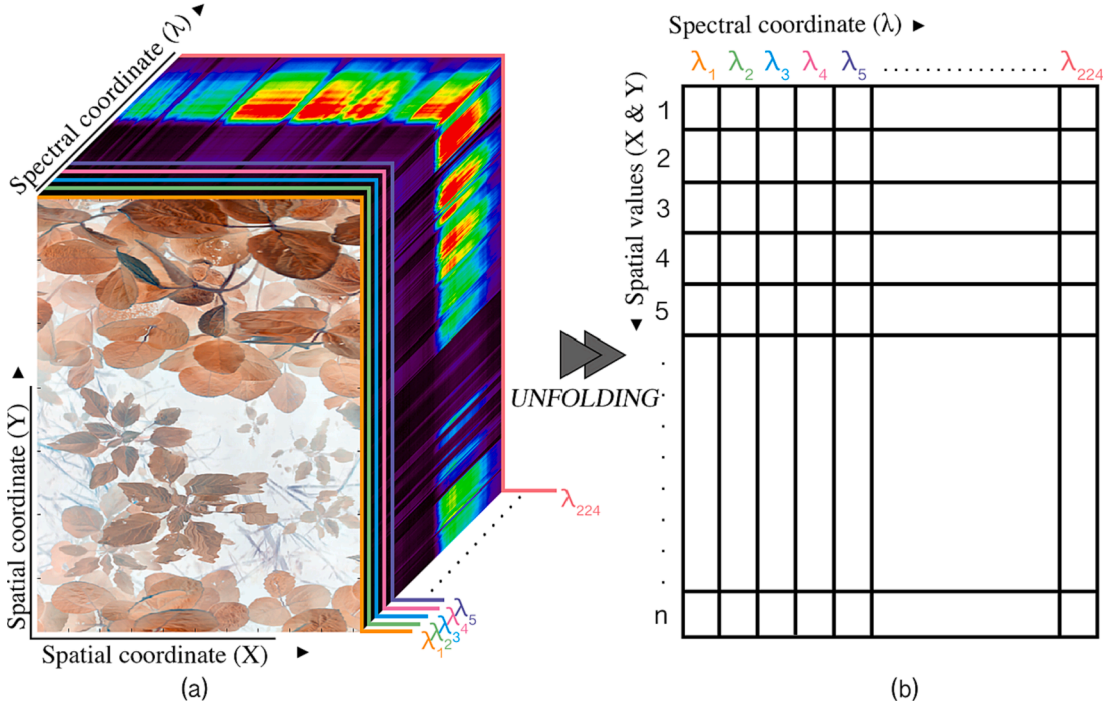

Fig. 5. The process of unfolding from a 3D cube to a 2D table. (a) The HSI data cube, and (b) The unfolded data in table format.

SNV, on the other hand, does not require a reference spectrum, and is calculated by mean-centering each sample and using spectrum-derived values for scaling:

$$\widetilde{x_i} = \frac{x_i - m_i}{\sigma_i} \tag{4}$$

where x_i is the spectrum, σ_i is the standard deviation, and m_i is the mean value of the sample. SNV and MSC are known as scatter correction methods, and a single-derivative method known as Savitzky-Golay (SG) was also applied in this work (Savitzky and Golay, 1964). The SG method adeptly merges differentiation and data smoothing within a single algorithm. By determining the slope at each data point via the derivative, the SG technique successfully mitigates noise present in the signal.

2.6. Hyperspectral image feature selection

HSI data contains redundant information due to the narrow distance between consecutive bands (Sun and Du, 2019). This increases processing time by overloading the machine with large amounts of data, and more importantly, is a factor for overfitting of the classification model (Ying, 2019). This has famously been known as "curse of dimensionality". To mitigate this issue, a feature selection approach was employed to identify the most significant features. Hyperspectral data cube containing all 224 wavelengths recorded by the sensor were refolded and used as input for feature selection. 10 most significant wavelengths were selected by the model based on the models' scoring. Four feature selection methods were used in this study, and the best was selected based on the F1 and MCC scores of the classifier. These methods include Recursive feature elimination (RFE), SelectFromModel (SFM), sequential forward selection (SFS), and sequential backward elimination (SBE). Python's Scikit-learn and MLxtend libraries were used for this task (Van Rossum and Drake, 2009, Pedregosa et al., 2011). RFE is a wrapper method that requires two input parameters (i.e., an estimator and the desired number of significant features). The RFE begins by training and fitting a model with the entire set of features and continues removing the least significant feature based on the result of the lowest feature score. A support vector machine (SVM) is used as the feature ranking criteria, and the RFE-SVM algorithm is used to score the features at each iteration. The process continues until the desired number of features have been achieved. SFM is similar to RFE and is also a meta-transformer like RFE, which means it selects features based on the importance of weights (Oikonomidis et al., 2022). However, it selects features based on a predefined importance measure (e.g., feature importance scores or coefficients) obtained from a specified estimator, which in this case was SVM (Wei et al., 2021). In SFS, features are added or removed sequentially depending on their classification rates, and all features are given as input. Next, the highest-performing features are added continuously to an empty feature set until their addition begins to increase the misclassification rate. Mathematically, this can be represented as input $Y = \{y_1, y_2, \ldots..,\ y_d\}$, where d represents the dimensions of the input features. The output can be represented as $X_k = \{x_j | j = 1,2,\cdots,k;\ x_j \in Y\}$, where $k = (0, 1, 2, \cdots, d)$. The algorithm was initialized by a null set of features, where k is the size of the feature subset that starts initially at 0. After initialization, a feature (x^+) was added to X_k based on its classification performance. This process was continued until k contained the number of desired features predetermined by the user:

$$x^+ = argmaxJ(X_k + x), where x \in Y - X_k \tag{5}$$

$$X_{k+1} = X_k + x^+ \tag{6}$$

$$k = k + 1 \tag{7}$$

Similarly, in SBE, all the features are given as input $Y = \{y_1, y_2, \cdots., y_d\}$, where the features are of d dimensions. Unlike SFS's null feature set at initialization, SBE was initialized by a feature set containing all the features, and in every iteration an omission (x^-) was made from the feature set $X_k = \{x_j | j = 1, 2, \cdots, k;\ x_j \in Y\}$, where $k\,(0, 1, 2, \cdots, d)$. This cycle was continued until the feature subset attains the desired number of features. The decision to remove a feature was made on the calculation that removing that feature (x^-) will increase the classification result.

$$x^- = argmaxJ(X_k - x), where x \in X_k \tag{8}$$

$$X_{k-1} = X_k - x^- \tag{9}$$

$$k = k - 1 \tag{10}$$

2.7. Dataset preparation for machine learning

Supervised ML includes a ground truth data as a label class in the input data set. This label class guides the ML during the algorithm training to create a relationship between classes and their respective features (Ayodele, 2010). In ML, the input data is divided into training, validation, and testing data. The testing data set remains separated from the ML and is only used to test the classifier's prediction performance. The classifier learns to predict these features using various probabilistic and non-probabilistic algorithms. There are multiple classifiers that help in supervised ML, and these classifiers are different in their approach to how they learn from input features and labels. Supervised ML was implemented using MATLAB's Classification Learner app (MATLAB and Statistics & Machine Learning Toolbox™ Release 2021b, The MathWorks, Inc. Natick, Massachusetts, United States). As is common practice for ML, data was divided as 20 % for validation, 60 % for training, and 20 % for testing. A comprehensive description of the dataset can be found in Table 1. Each image in this dataset was a 3-dimensional array composed of two spatial resolutions and one spectral resolution of 224 bands. The dataset, created by unfolding and combining all samples, consisted of 2.7 million instances (pixel values) and 224 features (columns). A class column was added to classify instances as either soybean or Palmer amaranth. The number of features was reduced to ten through a feature selection process before the dataset was used for training or testing. Nine models, including Decision Trees, Linear and Quadratic Discriminant Analysis, Logistic Regression, Naïve Bayes, K-Nearest Neighbor (KNN), Ensemble, Kernel Approximation, Support Vector Machine (SVM), and Neural Network Classifiers (NNC), were trained on four sets of features selected using RFE, SFM, SFS, and SBE. These models are well known supervised classifiers in the ML community (Singh et al., 2016). Fig. 6 summarizes the complete workflow of the hyperspectral image analysis.

2.8. Evaluation metrics

Evaluation metrics are used to determine the accuracy of a trained ML model for its prediction on testing data. Prediction accuracy, which is calculated as the number of correct predictions divided by the total number of samples, is often higher for imbalanced datasets. However, this metric does not consider the impact of false positives (FP) and false negatives (FN). In our case, a FP would be when the classifier classifies Palmer amaranth as soybean and a FN would be when the classifier classifies soybean as Palmer amaranth. Both cases are not favorable and should not be reflected in the accuracy. Precision and recall were utilized to limit the impact of potential errors. Precision reveals the positive predictions made by the classifier, which in our case would be correct Palmer amaranth predictions (true positives (TP)) by the labelled Palmer amaranth samples and incorrectly predicted Palmer amaranth as soybean samples (FP), whereas recall would be the amount of Palmer amaranth samples correctly predicted (TP) out of all the Palmer amaranth samples (TP and FN). The F1 evaluation metric is also used to justify the predictability of the classification models in supervised ML methods. The F1 score, Eq. (11), is the combination of precision and recall values to consider the amount of wrongly classified Palmer amaranth samples as soybean (FP) and wrongly classified soybean

Table 1
Number of samples and datapoints for Soybean and Palmer amaranth.

	Soybean	Palmer amaranth	Total
Total samples	211	371	582
Training samples	135	237	372
Validation samples	34	59	93
Testing samples	42	75	117
Train dataset instances (pixels)	701,606	1,020,543	1,722,149
Validation dataset instances (pixels)	175,401	255,136	430,537
Test dataset instances (pixels)	180,750	398,288	579,038

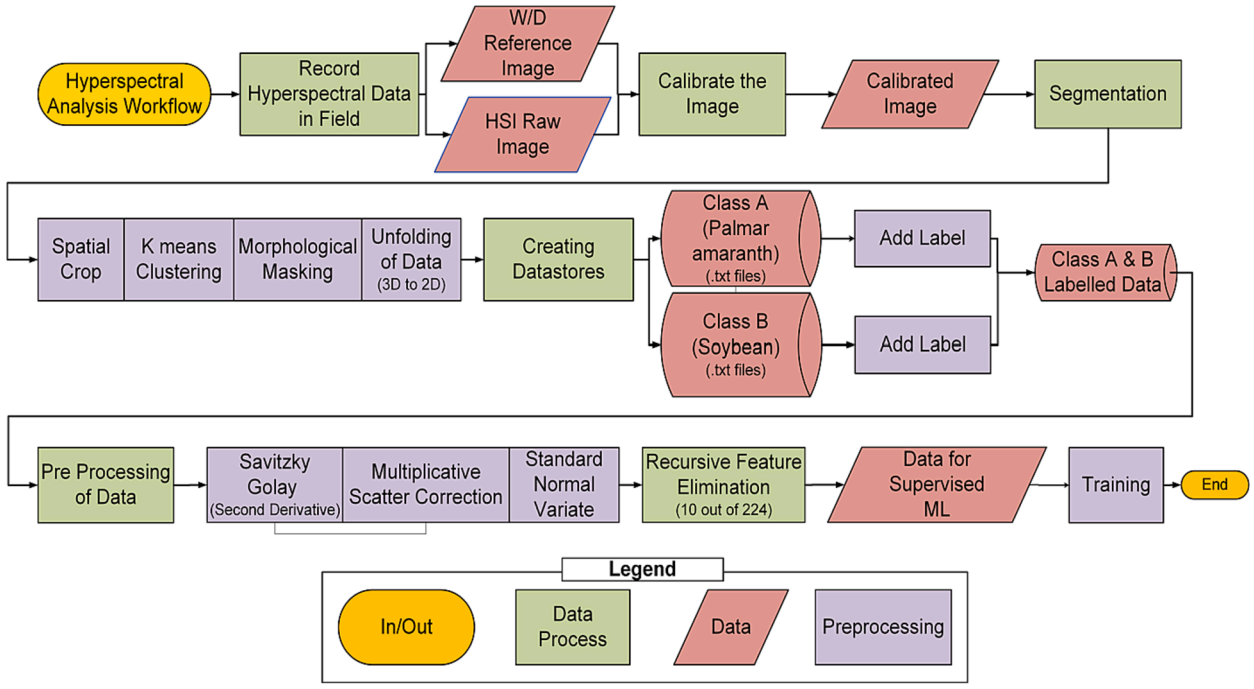

Fig. 6. Workflow for hyperspectral image analysis.

samples as Palmer amaranth (FN). It is a better metric of a classifier's performance, especially for an imbalanced dataset. Based on evaluations using the F1 score, recall, precision, and prediction accuracy, MCC, Eq. (12), was introduced in the study to measure the difference between predicted classes and actual classes, and, to study if it can better account for imbalanced dataset. Since the difference between the datasets for our two classes was significant. MCC has been studied to be a more robust evaluation metric for binary classifiers (Chicco and Jurman, 2020). MCC uses the chi-square statistics method and generates scores in the range of [-1, 1], where 1 is the best classifier. MCC along with the F1 score, recall, and precision, were utilized to evaluate the predictive power of the classifier.

$$\text{F1 Score} = 2 \times \frac{precision \times recall}{precision + recall} \tag{11}$$

$$\text{MCC} = \frac{(TP \times TN) - (FP \times FN)}{\sqrt{(TP + FP)(TP + FN)(TN + FP)(TN + FN)}} \tag{12}$$

2.9. Classification of soybean and palmar amaranth

The most effective classifier produced from our ML training was utilized to detect Palmer amaranth and soybean in a field image. A random image was selected and preprocessed, and background from the whole image was removed using K-means clustering. The image was then unfolded, and 10 significant wavebands from RFE were used in the data while removing the other bands. A prediction was made using the quadratic discriminant classifier (QDA). After the predictions were obtained, the image was transformed to its original dimensions and a logical mask was derived consisting of three numerical values corresponding to three categories: ground, Palmer amaranth, and soybean (Fig. 9). This logical mask was then converted to a two-dimensional array to generate the predicted image.

3. Results and discussion

3.1. Pre-processing and feature selection results for soybean and Palmer amaranth hyperspectral images

Pre-processing filters were applied in a forward feed manner. Savitzky-Golay 2nd derivative with a window size of 15, MSC, and SNV filters were applied to the data. These preprocessing methods were chosen because they yielded the best class separability between soybean and Palmer amaranth. Raw spectral signatures and preprocessed signatures of soybean and Palmer amaranth are shown in Fig. 7 (a) and (c), and the mean spectral signature are shown in Fig. 7 (b) and (d). As stated by Pan et al. (2015), these spectral signatures show the presence of chlorophyll absorption between 500 and 596 nm. Non-photochemical quenching processes were observed between 500 and 550 nm as suggested by Krezhova (2011). These processes exist to help the plant's photosynthesis in case of adverse light energy absorption (Müller et al., 2001).

The sudden peak in Fig. 7 (d) starting from 690 to 710 nm is associated with red edge reflection (Horler et al., 1983). The wavelengths from 700 nm to 1000 nm fall under the third overtone region, which is an excited state of molecules from the ground state (Osborne, 1993). This area witness's H_2O molecule stretching at 750 nm and 970 nm and CH, CH_2, and CH_3 stretching from 850 to 950 nm (Jamshidi et al., 2014). Features selected from SFS and SBE generated an MCC score of 0.84 and 0.81 for the highest performing classifier and an MCC score of 0.27 and 0.29 for the lowest performing classifiers. The best results were achieved with the features selected by RFE. The highest MCC score of 0.85 was obtained using the quadratic discriminant classifier, while the lowest MCC score of −0.371 was obtained using the cubic SVM. Therefore, RFE feature selection method with SVM estimator was used to train ML models. Ten wavelengths with the most significant information for classifying soybean and Palmer amaranth were selected. These features were 437 nm, 447 nm, 458 nm, 482 nm, 545 nm, 559 nm, 610 nm, 704 nm, 939 nm, and 976 nm. MSC and SNV were noted to increase classification accuracy in a study by Helland et al. (1995). Preprocessing steps similar to our study were used by Pu et al. (2015) to categorize lamb muscles showing a good predictive result of more than 80 %. Our finding

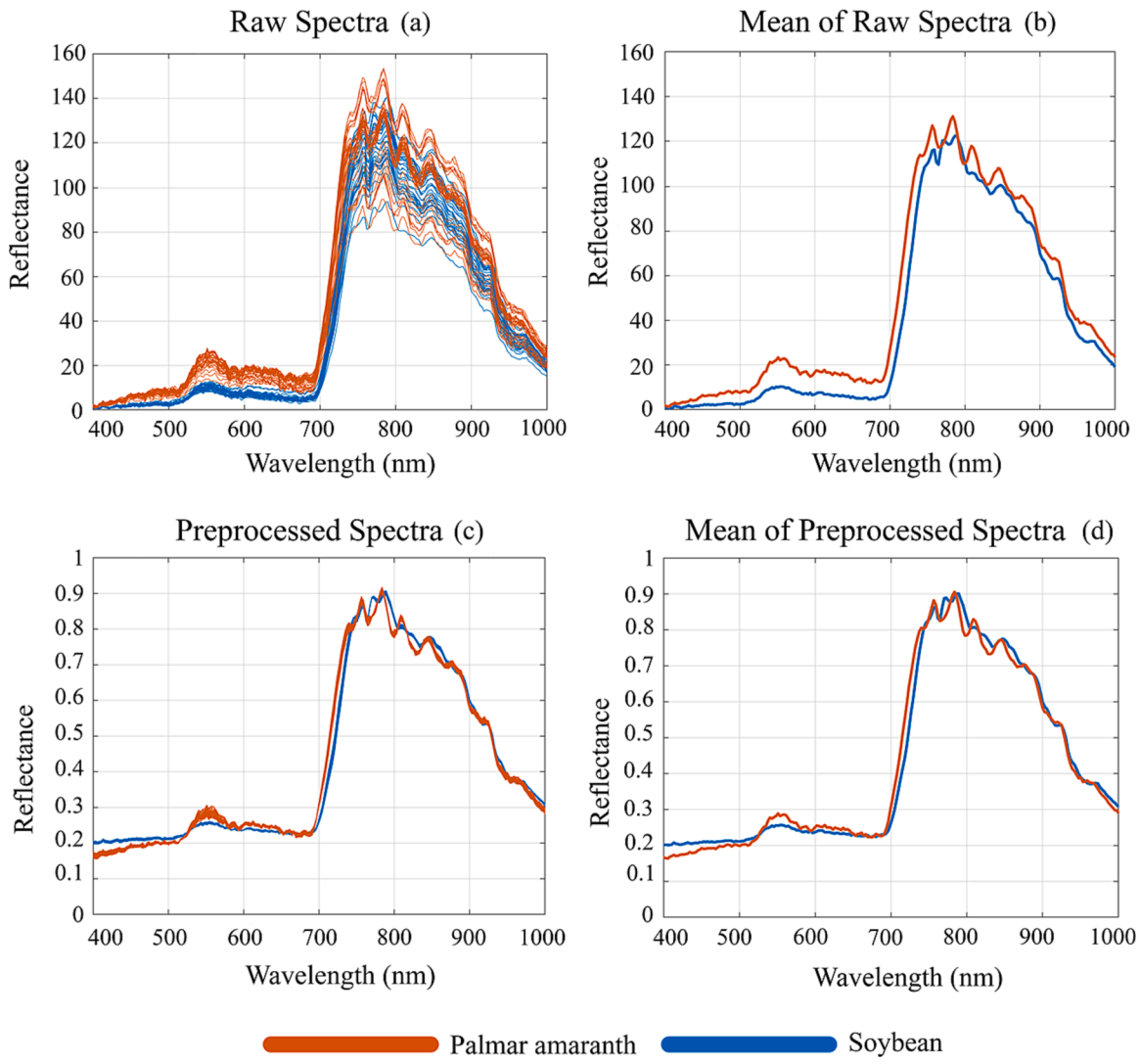

Fig. 7. A comparison of noisy raw data and data preprocessed using Savitzky-Golay, multiplicative scatter correction and standard normal variate methods.

of significant wavelengths in the range of VNIR is supported by the literature (Zhang et al., 2019). Zhang et al., (2012a) used the VNIR range of 400–795 nm with a Bayesian classifier for classification of tomato black nightshade and redroot pigweed weeds. Li et al. (2021) found a significant wavelength in the NIR region for detecting Ranunculus acris (giant buttercup) and Cirsium arvense (Californian thistle) in ryegrass and clover pastures. Gao et al. (2018) used a snapshot hyperspectral sensor with 25 bands in the range of 601–871 nm for maize and cirsium arvense rumex and convolvulus arvensis weeds. These findings along with the finding in this research support the claim that the NIR region has considerable potential to allow the differentiation between crops and weeds.

3.2. Classification results for soybean and Palmer amaranth from different machine-learning models

The predictability of Palmer amaranth and soybean according to different supervised machine-learning models and based on different evaluation metrics is shown in Table 2. The bi-layered and tri-layered neural networks had two and three hidden layers, respectively. There was no significant prediction accuracy improvement observed by increasing the number of hidden layers. The noticeable difference between the decision tree and the neural network's predictability is comparable to Goel et al. (2003) classification of corn with different stages of nitrogen and weeds. Similar to our findings, Goel et al. (2003) determined the performance of the neural network to be better than the decision trees. The MCC score for the Naïve Bayes classifier was 0.50, while its prediction accuracy was 78 %. In a similar study, Fletcher and Reddy (2016) generated hyperspectral data using a point spectrometer in a greenhouse to classify soybean and pigweed species. Their study received a kappa score of 0.93–0.97 with a random forest classifier. The simple linear, quadratic, and cubic SVM models performed poorly due to the lack of separability among classes. Conversely, the fine, medium, and coarse SVM models performed comparatively better. Medium gaussian SVM with scaling parameter of sqrt(predictors) was the second-best predictor, with prediction accuracy of 92 % and MCC of 0.80. While coarse gaussian had higher prediction accuracy than others which included the presence of FP and FN, justifying a lower MCC score. Ravikanth et al. (2015) classified seven contaminates in a wheat field, and were able to achieve classification accuracy of 79 %, 60.90 %, and 90.10 % for SVM, naïve bayes, and KNN, respectively, after similar preprocessing with SG, MSC, and SNV. A similar trend was observed in the SVM, KNN, and Naïve Bayes classifiers. For ensemble classifiers, while the model predictability ranged from 76 to 80 % and the MCC score ranged from 0.40 to 0.60, a significant difference was observed between the prediction accuracy and the MCC score. This is associated with the presence of a larger number of FP and FN in the classifier. The reason for the low MCC of the linear discriminant can be associated with

Table 2
Classifier performance for hyperspectral imagery features that were selected from recursive feature elimination, arranged from highest to lowest performance based on Matthew's correlation coefficient (MCC).

Classifier	ValidationAccuracy (%)	Prediction Accuracy (%)	Precision	Recall	F1	MCC
Quadratic Discriminant	**93.7**	**93.95**	**0.956**	**0.954**	**0.956**	**0.859**
Medium Gaussian SVM	97.1	92.58	0.956	0.935	0.945	0.830
Narrow Neural Network	96.8	91.67	0.944	0.934	0.939	0.807
Fine Gaussian SVM	97.8	91.66	0.987	0.942	0.94	0.805
Wide Neural Network	97.4	91.6	0.937	0.941	0.939	0.804
Bi-layered Neural Network	97.1	91.48	0.934	0.943	0.938	0.801
Medium Neural Network	97.1	91.19	0.941	0.93	0.936	0.796
Tri-layered Neural Network	97	91.21	0.935	0.937	0.936	0.795
Coarse Nearest Neighbor (KNN)	97.1	90.63	0.948	0.914	0.931	0.788
Cubic Nearest Neighbor (KNN)	97.9	90.75	0.939	0.926	0.932	0.786
Weighted Nearest Neighbor (KNN)	97.8	90.63	0.942	0.920	0.931	0.785
Medium Nearest Neighbor (KNN)	97.9	90.66	0.938	0.925	0.932	0.784
Coarse Gaussian SVM	90.04	95.80	0.947	0.906	0.926	0.776
Fine Nearest Neighbor (KNN)	97.9	89.53	0.932	0.914	0.923	0.759
Subspace KNN ensemble	96.7	86.62	0.896	0.911	0.904	0.685
Logistic Regression	92.5	86.38	0.898	0.905	0.901	0.681
Linear Discriminant	92.3	85.34	0.91	0.873	0.891	0.668
Fine Decision Tree	91.7	85.02	0.918	0.859	0.888	0.667
Boosted Trees Ensemble	92.7	80.84	0.896	0.816	0.854	0.582
Gaussian Naïve Bayes	77.2	78.27	0.901	0.768	0.829	0.548
Logistic regression kernel approximation	79.3	76.85	0.868	0.782	0.823	0.497
Subspace Discriminant Ensemble	90	76.21	0.844	0.802	0.823	0.463
SVM kernel approximation	89.4	5.34	0.832	0.804	0.818	0.438
Coarse Decision Tree	83.8	75.92	0.794	0.877	0.834	0.408
Medium Decision Tree	88.7	70.51	0.861	0.681	0.761	0.408
Linear SVM	72	65.26	0.733	0.779	0.755	0.160
Quadratic SVM	53	39.04	0.585	0.392	0.469	0.206
Cubic SVM	57.8	42.96	0.581	0.611	0.596	0.371

the difference in the precision and recall values. Quadratic discriminant performed best in classifying both classes, with a prediction score of 93.95 %, a precision of 0.956, a recall of 0.954, an F1 score of 0.956, and an MCC score of 0.859. Our findings indicate that the quadratic discriminant analysis is the most effective classifier, as it resulted in a reduction of both FP and FN in our prediction outcomes.

3.3. MCC vs F1 score: evaluation metric results for machine-learning models

The coarse decision tree model achieved an F1 score of 0.834, however, its Matthews Correlation Coefficient (MCC) score was only 0.408. This suggests the presence of large numbers of false positives and false negatives. A similar discrepancy between prediction accuracy and MCC score was observed in other low-performing models. This indicates that MCC is a more suitable metric for evaluating models on unbalanced datasets where false positives and false negatives can significantly impact prediction accuracy. Further evaluation results are presented in Table 2, and the confusion matrix for the quadratic discriminant classifier is illustrated in Fig. 8.

3.4. Prediction results using quadratic discriminant classifier on soybean and Palmer amaranth hyperspectral image

The quadratic discriminant classification of soybean and Palmer amaranth on a random image is shown in Fig. 9. The visible distortion in the prediction image is due to the motion of leaves due to wind while data recording was in process. This is an inherent disadvantage of using a pushbroom sensor but does not affect the data's spectral quality. This image was segmented using K-means clustering and unfolded to make the predictions. Ten significant wavebands selected from RFE were used in the prediction data. The prediction accuracy with the quadratic discriminant classifier was found 87.3 %. This image was then refolded using the logical mask generated during segmentation, and the prediction image was generated using the prediction class converted to the spatial dimension of the image.

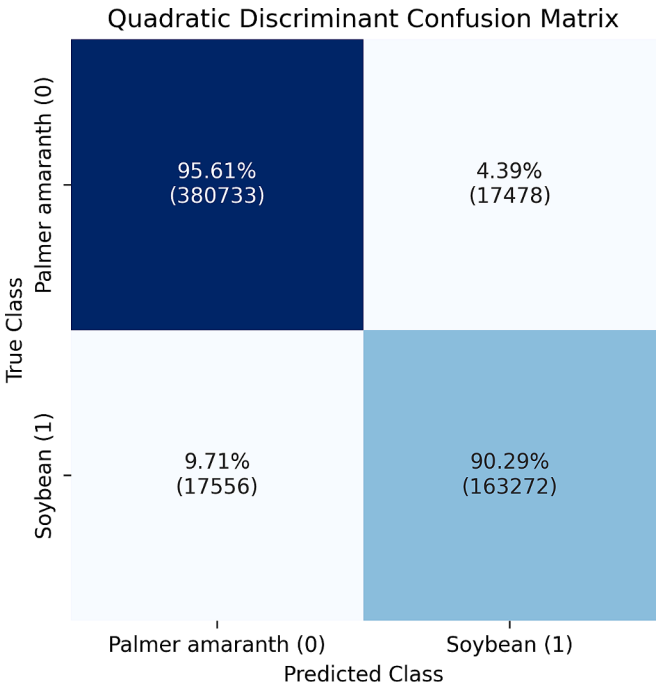

Fig. 8. Confusion matrix showing the number of pixels predicted as soybean and Palmer amaranth.

4. Conclusions

Differentiating crops from native weeds or differentiating between similar weed species growing in natural field conditions is a complex task, owing to multiple parameters. Class separability during labeling can be impacted by occluding leaves, and the quality of data collection is greatly impacted by constantly changing atmospheric conditions.

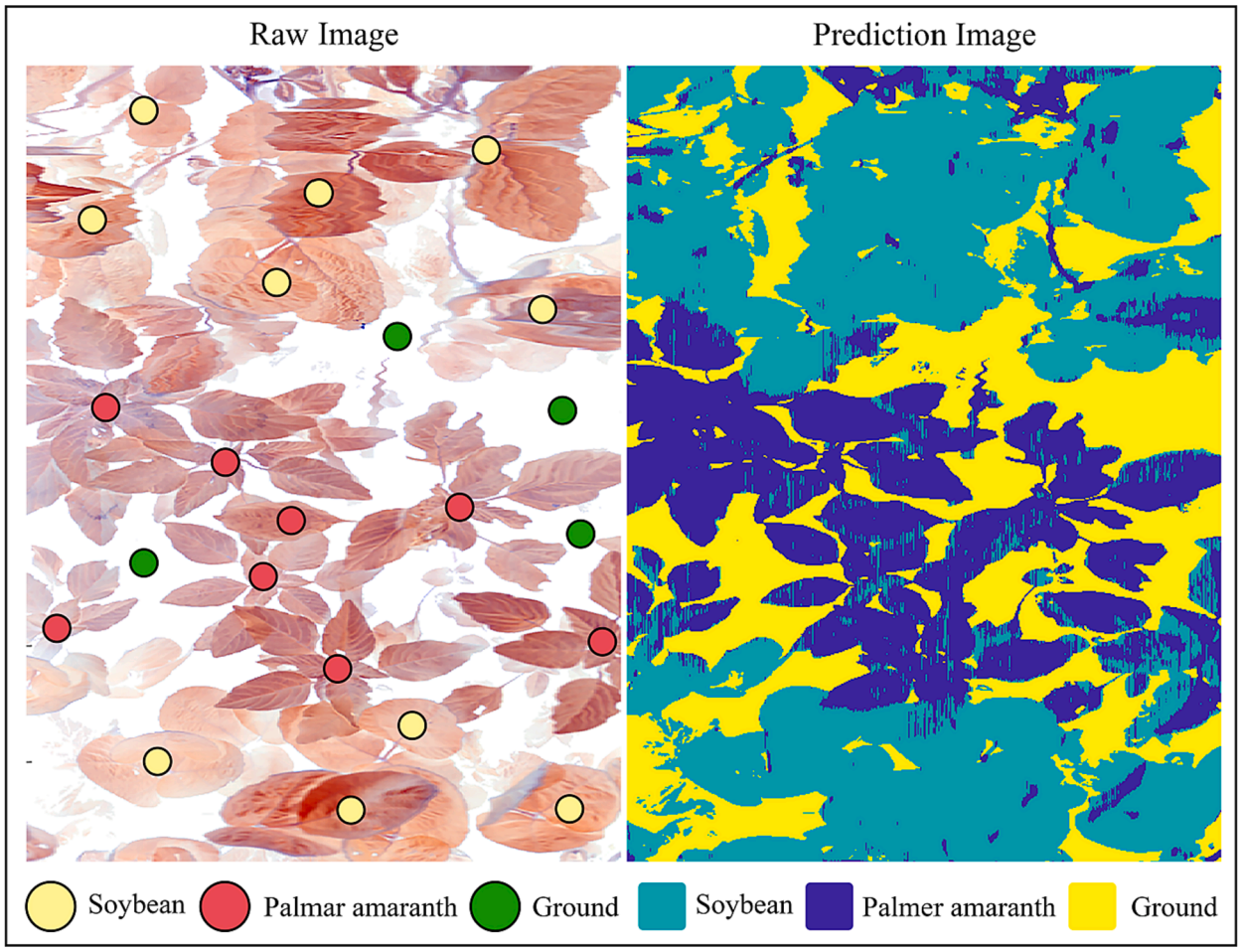

Fig. 9. The prediction image generated by quadratic discriminant model using the 10 significant wavebands selected using Recursive Feature Elimination.

Additionally, capturing images for classification across the entire field may be challenging. This research supports the claim that native Palmer amaranth weeds growing in field conditions can be differentiated from soybean crops using hyperspectral imagery. The best ML model in this study was quadratic discriminant, with a prediction accuracy of 93.90 %, an F1 score of 0.90, and an MCC score of 0.859. The classifier was tested on a random image of soybean and Palmer amaranth, and the resulting prediction accuracy was found to be 87.3 %. Our results conclude that classification of Palmer amaranth is not only possible but can generate useful results because of the dimensional richness of the hyperspectral data. Future work based on this study can include (1) the creation of a database for multiple weeds and crops for models that can classify multiple weeds. (2) A platform with autonomous navigation and data recording capability in the field. (3) Use of Field Programmable Gate Arrays (FPGA) and Graphical Processing Units (GPU) can be explored for real-time model deployment in field for early weed detection and management. Working toward a more real-time solution for weed detection using hyperspectral sensors can have promising applications in autonomous weed management machines.

CRediT authorship contribution statement

Billy Graham Ram: Data curation, Formal analysis, Methodology, Software, Validation, Visualization, Writing – original draft. **Yu Zhang:** Formal analysis, Investigation, Methodology, Resources, Supervision, Validation, Writing – review & editing. **Cristiano Costa:** . **Mohammed Raju Ahmed:** Methodology, Writing – review & editing. **Thomas Peters:** Resources, Writing – review & editing. **Amit Jhala:** Resources, Writing – review & editing. **Kirk Howatt:** Resources, Writing – review & editing. **Xin Sun:** Conceptualization, Data curation, Funding acquisition, Project administration, Resources, Supervision, Writing – review & editing.

Declaration of Competing Interest

The authors declare that they have no known competing financial interests or personal relationships that could have appeared to influence the work reported in this paper.

Data availability

Data will be made available on request.

Acknowledgements

This material is based on work partially supported by the U.S. Department of Agriculture, agreement number 58-6064-8-023. This work is/was supported by the USDA National Institute of Food and Agriculture, Hatch project number ND01487. The authors want to thank all the collaborators at the University of Nebraska-Lincoln that contributed the field for data collection in this research. The authors also want to thank the NDSU Plant Science and Agricultural and Biosystems Engineering department research specialists for their help in this study's field data collection coordination and on-site help for graduate student assistant guidance. Lastly, we would like to express our gratitude to Dr. Igathinathane Cannayen, faculty member of the Department of

Agricultural and Biosystems Engineering at NDSU, for his invaluable assistance in reviewing and providing guidance during the writing of this manuscript.

References

Atsmon, G., Nehurai, O., Kizel, F., Eizenberg, H., Nisim lati, r., 2022. Hyperspectral imaging facilitates early detection of Orobanche cumana below-ground parasitism on sunflower under field conditions. Comput. Electron. Agric. 196, 106881.

Ayodele, T.O., 2010. Types of machine learning algorithms. New Adv. Mach. Learn., 3, 19-48.

Basinger, N.T., Hestir, E.L., Jennings, K.M., Monks, D.W., Everman, W.J., Jordan, D.L., 2022. Detection of Palmer amaranth (*Amaranthus palmeri*) and large crabgrass (*Digitaria sanguinalis*) with in situ hyperspectral remote sensing. I. Effects of weed density and soybean presence. Weed Sci. 70, 198–212.

Bensch, C.N., Horak, M.J., Peterson, D., 2003. Interference of redroot pigweed (*Amaranthus retroflexus*), Palmer amaranth (*A. palmeri*), and common waterhemp (*A. rudis*) in soybean. Weed Sci. 51, 37–43.

Chahal, P.S., Aulakh, J.S., Jugulam, M., Jhala, A.J., 2015. Herbicide-Resistant Palmer amaranth (Amaranthus palmeri S. Wats.) in the United States — mechanisms of resistance, impact, and management. Herbicides, Agronomic Crops and Weed Biology.

Chicco, D., Jurman, G., 2020. The advantages of the Matthews correlation coefficient (MCC) over F1 score and accuracy in binary classification evaluation. BMC Genomics 21, 1–13.

Costa, C., Zhang, Y., Howatt, K., Ram, B., Stenger, J., Nowatzki, J., Bajwa, S., Sun, X., 2022. Palmer amaranth (*Amaranthus palmeri* S. Watson) and Soybean (*Glycine max* L.) classification in greenhouse using hyperspectral imaging and chemometrics methods. J. Agric. Saf. Health 65, 179–188.

Farooq, A., Hu, J., Jia, X., 2019. Analysis of spectral bands and spatial resolutions for weed classification via deep convolutional neural network. IEEE Geosci. Remote Sens. Lett. 16, 183–187.

Fernández Pierna, J.A., Vermeulen, P., Amand, O., Tossens, A., Dardenne, P., Baeten, V., 2012. NIR hyperspectral imaging spectroscopy and chemometrics for the detection of undesirable substances in food and feed. Chemometr. Intell. Laborat. Syst., 117, 233-239.

Fletcher, R.S., Reddy, K.N., 2016. Random forest and leaf multispectral reflectance data to differentiate three soybean varieties from two pigweeds. Comput. Electron. Agric. 128, 199–206.

Gao, J., Nuyttens, D., Lootens, P., He, Y., Pieters, J.G., 2018. Recognising weeds in a maize crop using a random forest machine-learning algorithm and near-infrared snapshot mosaic hyperspectral imagery. Biosyst. Eng. 170, 39–50.

Goel, P.K., Prasher, S.O., Patel, R.M., Landry, J.A., Bonnell, R.B., Viau, A.A., 2003. Classification of hyperspectral data by decision trees and artificial neural networks to identify weed stress and nitrogen status of corn. Comput. Electron. Agric. 39, 67–93.

Helland, I.S., Næs, T., Isaksson, T., 1995. Related versions of the multiplicative scatter correction method for preprocessing spectroscopic data. Chemom. Intel. Lab. Syst. 29, 233–241.

Horak, M.J., Loughin, T.M., 2000. Growth analysis of four *Amaranthus* species. Weed Sci. 48 (347–355), 9.

Horler, D.N.H., Dockray, M., Barber, J., Barringer, A.R., 1983. Red edge measurements for remotely sensing plant chlorophyll content. Adv. Space Res. 3, 273–277.

Jamshidi, B., Minaei, S., Mohajerani, E., Ghassemian, H., 2014. Prediction of soluble solids in oranges using visible/near-infrared spectroscopy: effect of peel. Int. J. Food Prop. 17, 1460–1468.

Klingaman, T.E., Oliver, L.R., 2017. Palmer Amaranth (Amaranthus palmeri) Interference in Soybeans (Glycine max). Weed Sci. 42, 523–527.

Krezhova, Y., 2011. Spectral remote sensing of the responses of soybean plants to environmental stresses. Soybean-Genetics and Novel Techniques for Yield Enhancement. InTech Publ 5, 215–265.

Li, Y., Al-Sarayreh, M., Irie, K., Hackell, D., Bourdot, G., Reis, M.M., Ghamkhar, K., 2021. Identification of weeds based on hyperspectral imaging and machine learning. Front. Plant Sci. 11.

Lu, B., Dao, P.D., Liu, J., He, Y., Shang, J., 2020. Recent advances of hyperspectral imaging technology and applications in agriculture. Remote Sens. (Basel) 12, 2659.

Martens, H., Jensen, S., Geladi, P., 1983. Multivariate linearity transformation for near-infrared reflectance spectrometry. Proceedings of the Nordic symposium on applied statistics, 1983. Stokkand Forlag Publishers Stavanger, Norway, 205-234.

Matzrafi, M., Herrmann, I., Nansen, C., Kliper, T., Zait, Y., Ignat, T., Siso, D., Rubin, B., Karnieli, A., Eizenberg, H., 2017. Hyperspectral Technologies for Assessing Seed Germination and Trifloxysulfuron-methyl Response in Amaranthus palmeri (Palmer Amaranth). Front. Plant Sci., 8.

Mishra, P., Asaari, M.S.M., Herrero-Langreo, A., Lohumi, S., Diezma, B., Scheunders, P., 2017. Close range hyperspectral imaging of plants: a review. Biosyst. Eng. 164, 49–67.

Mobaraki, N., Amigo, J.M., 2018. HYPER-Tools. A graphical user-friendly interface for hyperspectral image analysis. Chemom. Intel. Lab. Syst. 172, 174–187.

Monks, D.W., Oliver, L.R., 1988. Interactions between soybean (glycine max) cultivars and selected weeds. Weed Sci. 36, 770–774.

Müller, P., Li, X.-P., Niyogi, K.K., 2001. Non-photochemical quenching. A response to excess light energy1. Plant Physiol. 125, 1558–1566.

Noviyanto, A., Abdulla, W.H., 2019. Segmentation and calibration of hyperspectral imaging for honey analysis. Comput. Electron. Agric. 159, 129–139.

Oikonomidis, A., Catal, C., Kassahun, A., 2022. Hybrid deep learning-based models for crop yield prediction. Appl. Artif. Intell. 1–18.

Osborne, B.G., 1993. Practical NIR spectroscopy with applications in food and beverage analysis. Longman Scientific & Technical, p. 153.

Pan, W.-J., Wang, X., Deng, Y.-R., Li, J.-H., Chen, W., Chiang, J.Y., Yang, J.-B., Zheng, L., 2015. Nondestructive and intuitive determination of circadian chlorophyll rhythms in soybean leaves using multispectral imaging. Sci. Rep. 5, 11108.

Pavia, D.L., Lampman, G.M., Kriz, G.S., Vyvyan, J.A., 2014. Introduction to spectroscopy. Cengage learning.

Pedregosa, F., Varoquaux, G., Gramfort, A., Michel, V., Thirion, B., Grisel, O., Blondel, M., Prettenhofer, P., Weiss, R., Dubourg, V., 2011. Scikit-learn: machine learning in python. J. Mach. Learn. Res. 12, 2825–2830.

Piqueras, S., Burger, J., Tauler, R., de Juan, A., 2012. Relevant aspects of quantification and sample heterogeneity in hyperspectral image resolution. Chemom. Intel. Lab. Syst. 117, 169–182.

Pu, H., Xie, A., Sun, D.-W., Kamruzzaman, M., Ma, J., 2015. Application of wavelet analysis to spectral data for categorization of lamb muscles. Food Bioproc. Tech. 8, 1–16.

Ravikanth, L., Singh, C.B., Jayas, D.S., White, N.D.G., 2015. Classification of contaminants from wheat using near-infrared hyperspectral imaging. Biosyst. Eng. 135, 73–86.

Rinnan, Å., Nørgaard, L., van den Berg, F., Thygesen, J., Bro, R., Engelsen, S.B., 2009. Data pre-processing. Infrared Spectroscopy for Food Quality Analysis and Control 29–50.

Savitzky, A., Golay, M.J., 1964. Smoothing and differentiation of data by simplified least squares procedures. Anal. Chem. 36, 1627–1639.

Singh, A., Thakur, N., Sharma, A., 2016. A review of supervised machine learning algorithms. 2016 3rd International Conference on Computing for Sustainable Global Development (INDIACom), 16-18, 1310–1315.

Sun, W., Du, Q., 2019. Hyperspectral band selection: a review. IEEE Geosci. Remote Sens. Mag. 7, 118–139.

Thomas, S., Kuska, M.T., Bohnenkamp, D., Brugger, A., Alisaac, E., Wahabzada, M., Behmann, J., Mahlein, A.-K., 2018. Benefits of hyperspectral imaging for plant disease detection and plant protection: a technical perspective. J. Plant Dis. Prot. 125, 5–20.

van Rossum, G., Drake, F.L., 2009. Python 3 Reference Manual. CreateSpace.

Wei, X., Johnson, M.A., Langston, D.B., Mehl, H.L., Li, S., 2021. Identifying optimal wavelengths as disease signatures using hyperspectral sensor and machine learning. Remote Sens. (Basel) 13, 2833.

Xu, K., Zhu, Y., Cao, W., Jiang, X., Jiang, Z., Li, S., Ni, J., 2021. Multi-modal deep learning for weeds detection in wheat field based on RGB-D images. Frontiers Plant Sci. 12.

Ying, X. 2019. An overview of overfitting and its solutions. J. Phys.: Conf. Series, 1168, 022022.

Yoon, S.-C., Park, B., 2015. Hyperspectral Image Processing Methods. In: Park, B., Lu, R. (eds.) Hyperspectral Imaging Technology in Food and Agriculture. Springer New York, New York, NY.

Zhang, Y., Slaughter, D.C., Staab, E.S., 2012a. Robust hyperspectral vision-based classification for multi-season weed mapping. ISPRS J. Photogramm. Remote Sens. 69, 65–73.

Zhang, Y., Staab, E.S., Slaughter, D.C., Giles, D.K., Downey, D., 2012b. Automated weed control in organic row crops using hyperspectral species identification and thermal micro-dosing. Crop Prot. 41, 96–105.

Zhang, Y., Gao, J., Cen, H., Lu, Y., Yu, X., He, Y., Pieters, J.G., 2019. Automated spectral feature extraction from hyperspectral images to differentiate weedy rice and barnyard grass from a rice crop. Comput. Electron. Agric. 159, 42–49.